A tetrairon(III) single-molecule magnet and its solvatomorphs: synthesis, crystal structures and vapor-phase processing

A tetrairon(III) single-molecule magnet and its solvatomorphs: synthesis, crystal structures and vapor-phase processing

Andrea Cornia[a,*], Andrea Nava[a,b], Valeria Lanzilotto[c,1], Giordano Poneti[d], Matteo Mannini[c], Roberta Sessoli[c]

[a]Department of Chemical and Geological Sciences and INSTM Research Unit, University of Modena and Reggio Emilia, Via G. Campi 103, 41125 Modena, Italy.
[b]Department of Physics, Informatics and Mathematics, University of Modena and Reggio Emilia, Via G. Campi 213/a, 41125 Modena, Italy.
[c]Department of Chemistry "U. Schiff" and INSTM Research Unit, University of Florence, Via della Lastruccia 3-13, 50019 Sesto Fiorentino (FI), Italy.
[d]Instituto de Química, Universidade Federal do Rio de Janeiro, Avenida Athos da Silveira Ramos, 149, Centro de Tecnologia – Cidade Universitária, 21941-909 Rio de Janeiro, Brazil.

[1]Present address: Department of Chemistry, Sapienza University of Rome, Piazzale Aldo Moro 5, 00185 Rome, Italy.
[*]Corresponding author. Tel.: +39 (0) 59 2058645. *E-mail address:* acornia@unimore.it.

Abstract

With the aim of investigating the impact of lattice solvent on the processability of tetrairon(III) single-molecule magnets by thermal sublimation, two new solvatomorphs of $[Fe_4(L^{Ph})_2(dpm)_6]$ (**1**) were prepared and structurally characterized along with unsolvated **1** (H_3L^{Ph} = 2-(hydroxymethyl)-2-phenylpropane-1,3-diol, Hdpm = dipivaloylmethane). All solvatomorphs crystallize in the *C*2/*c* space-group whereas solvent-free **1** belongs to a different space group ($P2_1/c$). The pitch of the propeller-like tetrairon(III) molecules is distinctly different in solvated vs. unsolvated phases, highlighting the effect of intermolecular interactions and crystal packing. The compounds sublimate at 450 - 490 K (in high vacuum conditions ~ 10^{-6}-10^{-7} mbar) affording thick deposits which display different crystallinity depending on the particular starting material used. However, all sublimated samples retain slow magnetic relaxation with thermal activation parameters comparable to those of microcrystalline **1**. The results indicate that factors other than mere molecular structure have a limited influence on the processability of these materials by thermal sublimation.

Keywords

Single-molecule magnet; Iron; Sublimation; Thin film; Magnetization dynamics

1. Introduction

The processing of single-molecule magnets (SMMs) into films with variable thickness, down to monolayers or sub-monolayers [1,2], is motivated by the perspective use of these magnetically bistable materials in spintronic devices [3] or as individually addressable, surface-supported magnetic bits [4]. A major breakthrough in the field was the recent discovery that some organometallic monodysprosium(III) SMMs retain a memory effect above the normal boiling point of liquid dinitrogen [5–7]. The real application potential [8] of most SMMs, however, is severely limited by their instability under the processing methods customarily used in spintronics, above all thermal sublimation in high vacuum (HV). Some mononuclear SMMs withstand sublimation, like those of the $LnPc_2$ [9–14] and Ln(trensal) [15–17] families, as well as a few other lanthanoid (Ln) complexes [18–20] (H_2Pc = phthalocyanine, H_3trensal = 2,2′,2″-tris(salicylideneimino)triethylamine). Polynuclear SMMs suitable for vapour phase processing are also known and include triple-decker Ln_2Pc_3 derivatives [9,11,21], a Dy_2 species [22,23] and endohedral fullerenes [24].

Some tetrairon(III) compounds with formula $[Fe_4(L^R)_2(dpm)_6]\cdot$solv are also sublimable (Hdpm = dipivaloylmethane, solv = lattice solvent). This family of SMMs have a propeller-like structure enveloped by a bulky shell of twelve *t*Bu groups and held together by two tripodal $(L^R)^{3-}$ ligands (H_3L^R = 2-R-2-(hydroxymethyl)propane-1,3-diol). A number of derivatives have been prepared and characterized which differ in the R substituent and/or in the presence and nature of lattice solvent [25]. The phenyl derivative (**1**, R = Ph), for instance, is best isolated as the diethylether solvate **1**·Et_2O [26]. This compound was sublimated at 500 ± 10 K in HV (10^{-7} mbar) to give ~100 nm thick deposits which showed slow magnetic relaxation similar to the pristine material [27]. The same processing technique operated in Ultra-HV was used with success to prepare monolayers and submonolayers of **1** on Au(111) [28,29], Cu(100) [29] and Cu_2N/Cu(100) [29,30] surfaces. These studies indicated that structurally and functionally intact Fe_4 complexes can be transferred onto the surface, as proved by on-surface magnetometry [28], although smaller fragments are often co-deposited [29]. Fluorinated variants of **1** [31,32] and the derivative with R = CH_2SCH_3, isolated as the hemidiethylether solvate **2**·0.5Et_2O [33], are also sublimable.

In an attempt to clarify whether factors other than mere molecular structure influence processability, we have prepared two new solvatomorphs of **1**, namely **1**·C_7H_8 and **1**·2CCl_4, which are isostructural with previously reported **1**·Et_2O [26] and **1**·C_6H_6 [34]. In the course of this study, we were also able to isolate solvent-free **1**, which however crystallizes in a different space group than do solvated phases. We found that all these compounds with R = Ph show similar sublimation temperatures in HV and afford deposits with different crystallinity depending on the used pristine material. However, all sublimated samples retain slow magnetic relaxation with thermal activation parameters similar to microcrystalline **1**.

2. Experimental

General procedures. All synthetic operations were conducted with exclusion of moisture using reagent grade solvents, unless otherwise stated. Methanol was carefully dried over $Mg(OMe)_2$ and distilled prior to use [35,36], while pentachloroethane was purified and distilled as described in ref. [35]. Compounds **1**·Et_2O and **1**·C_6H_6 were prepared as previously reported [26,34]. Microanalytical CHN determinations were carried out on microcrystalline samples of all compounds using a Carlo Erba EA1110 CHNS-O automatic analyzer.

Synthesis of [$Fe_4(L^{Ph})_2(dpm)_6$]·C_7H_8 (**1**·C_7H_8): **1**·Et_2O (0.037 g, 0.021 mmol) was dissolved in 0.5 mL of toluene. Slow evaporation over vaseline oil (4 mL) overnight under reduced pressure (440 torr) gave orange-red crystals (0.029 g, 78% yield). Anal. Calcd (%) for $C_{93}H_{144}Fe_4O_{18}$ (1773.51): C, 62.98; H, 8.18. Found: C, 62.61; H, 8.10.

Synthesis of [$Fe_4(L^{Ph})_2(dpm)_6$]·2CCl_4 (**1**·2CCl_4): **1**·Et_2O (0.027 g, 0.015 mmol) was dissolved in 0.5 mL of tetrachloromethane. Slow vapor diffusion of methanol (5 mL) gave orange-red crystals after three days (0.026 g, 85% yield). Anal. Calcd (%) for $C_{88}H_{136}Cl_8Fe_4O_{18}$ (1989.01): C, 53.14; H, 6.89. Found: C, 52.96; H, 6.62.

Synthesis of [$Fe_4(L^{Ph})_2(dpm)_6$] (1): **1**·Et_2O (0.056 g, 0.032 mmol) was dissolved in 2 mL of pentachloroethane. Slow evaporation over vaseline oil (10 mL) over two weeks under reduced pressure (260 torr) gave orange-red crystals (0.044 g, 82% yield). Anal. Calcd (%) for $C_{86}H_{136}Fe_4O_{18}$ (1681.37): C, 61.43; H, 8.15. Found: C, 61.32; H, 8.20.

X-ray Crystallography. Single-crystal X-ray structure determinations on **1**·C_7H_8 and **1**·2CCl_4 were carried out at 140(2) K on a Bruker-Nonius X8APEX diffractometer equipped with Mo-Kα generator, area detector and Kryoflex liquid dinitrogen cryostat. Measurements on **1** were conducted on the same instrument at 150(2) and 298(2) K. The structures were solved and refined on F_o^2 by standard methods, using SIR92 [37] and SHELXL-97, SHELXL-2014/7 or SHELXL-2018/3 [38] softwares and the WINGX suite [39]. All nonhydrogen atoms were refined anisotropically, unless otherwise noted, while H atoms were added in idealized positions, allowed to ride on the parent C atoms and treated isotropically with $U(H) = 1.5U_{eq}(C)$ for methyl hydrogens and $U(H) = 1.2U_{eq}(C)$ for the remaining H atoms. When deemed necessary, anisotropic displacement parameters (ADPs) were subject to rigid body (DELU) and/or quasi-isotropy (ISOR) restraints.

In **1**·C_7H_8, one *t*Bu group shows rotational disorder over two positions with 0.580(8):0.420(8) occupancies. The two components were forced to have a similar geometry (SAME) and their quaternary C atoms were assigned the same ADP. Toluene molecule is disordered around a twofold axis and was refined with 0.5 occupancy and a unique isotropic displacement parameter (IDP) for its C atoms. The C skeleton was restrained to have *mmm* symmetry, with a regular hexagonal geometry (C–C = 1.39 Å) for the phenyl ring and a C-CH_3 distance of 1.51(1) Å.

In **1**·2CCl_4, two *t*Bu groups show rotational disorder over three and two positions, respectively, with 0.551(3):0.197(3):0.252(3) and 0.753(6):0.247(6) occupancies, respectively. Minority *t*Bu groups were forced to have a similar geometry to a reference, non disordered *tert*-butyl in the structure (SAME). Their quaternary C atoms were constrained to have the same ADP as those of the corresponding majority component, and a common IDP was assigned to their methyl carbons. Restraints (SADI) were also applied to the C(O)-$C(CH_3)_3$ distances involving disordered *t*Bu groups. Three positions were resolved for the disordered CCl_4 molecule, with refined occupancies 0.734(2):0.131(2):0.135(2), constrained to sum up to unity. The minority components were forced to have a similar geometry (SAME) to the majority one and were treated isotropically, with one common displacement parameter for Cl and one for C atoms. The latter was restrained to be similar to that of the majority component (SIMU).

In the structure of **1** at 150(2) K one *t*Bu group shows rotational disorder over two positions with 0.846(5):0.154(5) occupancies. The two components were restrained to have a similar geometry (SAME) and quaternary C atoms with the same ADPs. The same IDP was assigned to the methyl carbons of the minority component. The room-temperature structure of **1**, determined on the same crystal, showed very elongated ADPs for the methyl carbons of most *t*Bu groups and converged to higher *R*-indices. A few C-CH_3 distances within *t*Bu groups were restrained to 1.51(1) Å (DFIX). Crystal data and refinement parameters for the three low-temperature structures described in this paper are given in Table S1. Graphics utilized ORTEP-3 for Windows v2014.1 [39] and POV-Ray for Windows v3.7 [40]. CCDC 2113116-2113119 contain the supplementary crystallographic data for this paper. These data can be obtained free of charge from The Cambridge Crystallographic Data Centre via www.ccdc.cam.ac.uk/data_request/cif.

Thermal sublimation. Thermal sublimation of **1**·C_7H_8, **1**·2CCl_4, **1**·C_6H_6, and unsolvated **1** was performed in HV conditions (P_{base} = 10^{-6} - 10^{-7} mbar) from a quartz crucible resistively heated up to the sublimation temperature of 450 - 490 K (temperature was monitored by a K-type thermocouple inserted into the crucible). Film growth was performed on a support (mica disk) covered with a Teflon® tape by keeping the powders at the sublimation temperature for ca. 2 days (**1**·C_7H_8), 4 days (**1**·2CCl_4), 18 h (**1**·C_6H_6), and 27 h (**1**). The mass of the deposits was 1.52 mg (**1**·C_7H_8), 1.46 mg (**1**·2CCl_4), 0.74 mg (**1**·C_6H_6), and 0.90 mg (**1**), and was measured by difference ($W_{(Teflon® + deposit)} - W_{Teflon®}$). As for the films thickness, the deposition rate was checked before and after deposition by a quartz crystal microbalance (QCM). However, after long-lasting processing the deposition rate usually depletes and the QCM-based thickness evaluation was only possible for **1**·C_6H_6, ca. 500 nm. By using the mass and thickness values of **1**·C_6H_6, we estimated a thickness of about 600 nm for **1** and ca. 1000 nm for **1**·2CCl_4 and **1**·C_7H_8.

X-ray Powder Diffraction. X-Ray powder diffraction data were acquired on the sublimated samples using a Bruker New D8 Advance DAVINCI diffractometer in a theta-theta configuration equipped with a linear detector. The scans were collected in the 5-20° range of 2θ with Cu-Kα radiation (λ = 1.540 Å). Powder patterns were simulated with Mercury 2021.1.0 [41] using a full-width-at-half-maximum of 0.1° in 2θ.

Magnetic measurements. Alternating current (AC) magnetic investigations in the frequency range ν = 10-1000 Hz were performed on a Quantum Design MPMS instrument, using an oscillating field amplitude of 1-3 Oe and working in both zero and 1 kOe applied static fields (H_{DC}). Measurements were carried out on a grinded and pelletized microcrystalline sample of **1** wrapped in Teflon® tape, and on sublimated deposits prepared from **1**·C_7H_8, **1**·$2CCl_4$, **1**·C_6H_6, and unsolvated **1**, collected on Teflon® tape. In-phase and out-of-phase molar susceptibilities (hereafter indicated as χ_M' and χ_M'', respectively) were calculated using a molar mass of 1681.35 g/mol, as appropriate for unsolvated **1**. The data were analysed within the extended Debye model [42], in which a maximum in χ_M'' is observed when the relaxation time τ equals $\omega^{-1} = (2\pi\nu)^{-1}$ and allowance is made for a distribution of relaxation times described by parameter α. The value of τ at each temperature was determined by fitting the frequency dependence of χ_M'' to equation (1):

$$\chi_M''(\omega) = (\chi_T - \chi_S)\frac{(\omega\tau)^{1-\alpha}\cos\frac{\pi\alpha}{2}}{1+2(\omega\tau)^{1-\alpha}\sin\frac{\pi\alpha}{2}+(\omega\tau)^{2-2\alpha}} \quad (1)$$

where χ_T and χ_S are the isothermal and adiabatic molar susceptibilities, *i.e.* the susceptibilities observed in the two limiting cases $\nu \to 0$ and $\nu \to \infty$, respectively. The individual values of χ_T and χ_S, as well as a more reliable value of α, were evaluated by fitting isothermal $\chi_M''(\chi_M')$ data (Cole-Cole plot) [42] to equation (2):

$$\chi_M''(\chi_M') = -\frac{\chi_T - \chi_S}{2}\tan\frac{\pi\alpha}{2} + \left[\left(\frac{\chi_T - \chi_S}{2}\tan\frac{\pi\alpha}{2}\right)^2 + (\chi_M' - \chi_S)(\chi_T - \chi_M')\right]^{1/2} \quad (2)$$

The temperature dependence of the relaxation time was then fitted to Arrhenius equation:

$$\tau(T) = \tau_0\exp[\Delta/(k_BT)] \quad (3)$$

where Δ is the effective energy barrier to magnetic moment reversal, τ_0 is a pre-exponential factor and k_B is the Boltzmann constant.

3. Results and discussion

Synthesis and X-ray structures. Crystalline solvates of **1** with toluene (**1**·C_7H_8), tetrachloromethane (**1**·2CCl_4) and benzene (**1**·C_6H_6) [34] were obtained by recrystallizing **1**·Et_2O [26] from appropriate solvents. The unsolvated form **1** was first obtained as a byproduct of the synthesis of **1**·Et_2O, when the methanol-rich mother solution recovered after isolation of the compound was subject to further diffusion of methanol vapors for several weeks. These solvent-free crystals were then deliberately prepared by recrystallizing **1**·Et_2O from freshly-distilled pentachloroethane, a bulkier solvent.

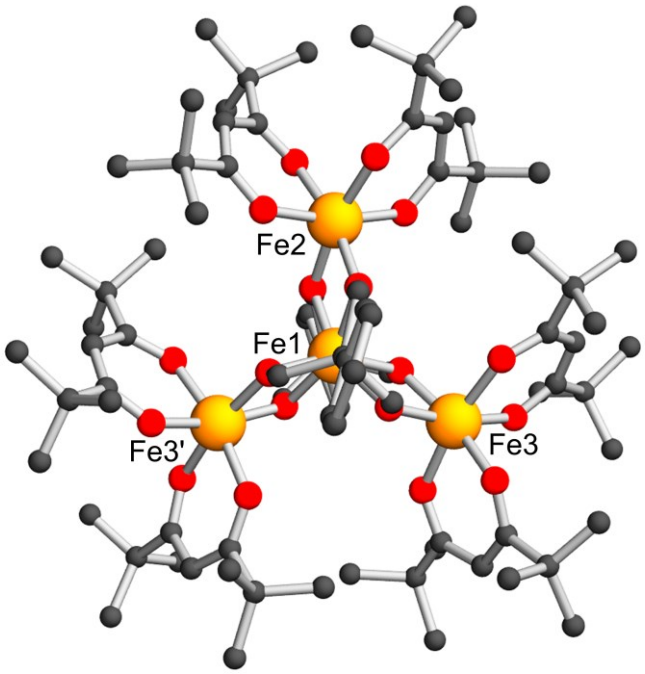

Fig. 1. Molecular structure of **1** in **1**·C_7H_8, viewed approximately normal to the molecular plane. Color code: orange = Fe, red = O, grey = C. The lattice toluene molecule, disorder effects and H atoms are omitted for clarity.

The X-ray structure of **1** in **1**·C_7H_8 is displayed in Fig. 1 as an example. The four metals exhibit a metal-centred triangular arrangement, with the two tripodal $(L^{Ph})^{3-}$ ligands bridging the central (Fe1) and peripheral (Fe2, Fe3, Fe3′) metals, and the six dpm^- anions providing terminal ligation to Fe2, Fe3 and Fe3′. **1**·C_7H_8 and all known solvated phases of **1** belong to monoclinic space group *C*2/*c* and their crystal structure entails four tetrairon(III) molecules per unit cell. The asymmetric unit includes half a tetrairon(III) complex, with two iron(III) ions (Fe1 and Fe2) located on a twofold axis. Consequently, the Fe_4 molecules have crystallographically imposed twofold symmetry and the four metal centers are exactly coplanar. Selected geometrical parameters are gathered in Table 1 together with those of **1**·Et_2O [26] and **1**·C_6H_6 [34] for comparison (a more complete listing is available in Table S2). Within the series of solvated phases, molecular geometry undergoes only minor variations

as a function of lattice solvent. An especially important geometrical parameter is the inclination (γ_{cp}) of each $Fe_c(O)_2Fe_p$ (mean) plane with respect to the (mean) plane through the four metals (here Fe_c and Fe_p denote the central and peripheral metals, respectively). The average value of γ_{cp} in a molecule is referred to as the "helical pitch" (γ) of the propeller-like structure. In the four solvates of **1**, the inclination values are remarkably similar within each compound and in different solvatomorphs (68.5-68.8°). The trigonal distortion parameters θ and ϕ for Fe_c are also very close [25,43,44].

Of course, because of the centrosymmetric space group, the crystals are racemic mixtures of right- and left-handed propellers. Solvent molecules reside in four symmetry-equivalent cavities per unit cell, located around twofold axes and showing individual volumes of 290, 345, 270 and 302 Å^3 in the structures of **1**·C_7H_8, **1**·2CCl_4, **1**·Et_2O [26], and **1**·C_6H_6 [34], respectively.

Table 1. Selected geometrical parameters in compounds **1**·C_7H_8 (at 140 K), **1**·2CCl_4 (at 140 K), **1**·Et_2O (at 203 K), **1**·C_6H_6 (at 120 K) and **1** (at 150 K)

		1·C_7H_8	**1**·2CCl_4	**1**·Et_2O [a]	**1**·C_6H_6 [b]
Fe1···Fe2 (Å)		3.0797(6)	3.0824(6)	3.0780(8)	3.0789(8)
Fe1···Fe3 (Å)		3.0783(4)	3.0780(4)	3.0726(6)	3.0764(5)
θ (°) [c]		54.21	54.19	54.20	54.18
ϕ (°) [c]		32.76	32.74	32.51	32.62
γ_{cp} (°)	$Fe1(O)_2Fe2$	68.51(5)	68.72(6)	68.79(7)	68.77(8)
	$Fe1(O)_2Fe3$	68.69(4)	68.64(5)	68.77(6)	68.71(6)
γ (°) [d]		68.63	68.67	68.78	68.73

	1, mol A			**1**, mol B		
Fe_c···Fe_p (Å)	Fe1···Fe2 3.0736(4)	Fe1···Fe3 3.0917(4)	Fe1···Fe4 3.0857(4)	Fe5···Fe6 3.0776(5)	Fe5···Fe7 3.0833(5)	Fe5···Fe8 3.0848(4)
θ (°) [c]	53.95			53.91		
ϕ (°) [c]	30.51			30.79		
γ_{cp} (°)	$Fe1(O)_2Fe2$ 70.61(4)	$Fe1(O)_2Fe3$ 69.33(4)	$Fe1(O)_2Fe4$ 70.41(4)	$Fe5(O)_2Fe6$ 70.73(4)	$Fe5(O)_2Fe7$ 69.86(4)	$Fe5(O)_2Fe8$ 69.37(4)
γ (°) [d]	70.12			69.99		

[a]Data taken from Ref.[26]. [b]Data taken from Ref.[34]. [c]The angles θ and ϕ describe the distortion of the coordination sphere of Fe_c (averaged to D_3 symmetry) by trigonal compression/elongation and trigonal rotation, respectively. The extent of distortion is measured by the deviation of these angles from octahedral values (54.74 and 60°, respectively). [d]Average value of γ_{cp}. For details, see Refs. [25,43,44].

Crystals of unsolvated **1** belong to centrosymmetric monoclinic space group $P2_1/c$; in this case, eight tetrairon(III) molecules are present in the unit cell. The asymmetric unit in fact contains two

crystallographically independent Fe_4 complexes (mol A: Fe1–Fe4; mol B: Fe5–Fe8) which differ in the conformation of *t*Bu and Ph substituents (Fig. 2). The four Fe atoms in each molecule lie on the same plane within 0.0011 (mol A) and 0.0030 Å (mol B), and the two molecules are almost coplanar (the average planes through the metals form a dihedral angle of 8.91(1)°). As shown in Tables 1 and S2, mol A and mol B have very similar metrical parameters, with γ_{cp} varying from 69.3 to 70.6° in mol A and from 69.4 to 70.7° in mol B, and a virtually identical γ (70.1 and 70.0°, respectively). Notably, the helical pitch is distinctly larger than in the solvate series (68.6-68.8°). Because of the correlation between γ and ϕ [43], the distortion of the coordination sphere of Fe_c by trigonal rotation is also approximately 2° larger than in the solvated phases (ϕ = 30.5-30.8° vs 32.5-32.8°). Since the tetrairon(III) molecule remains exactly the same, the observed differences prove that intermolecular interactions and crystal-packing effects play an important role in determining molecular geometry [43]. The unit cell of **1** contains 4.7% of solvent-accessible voids, which individually do not exceed 83 $Å^3$ and are thus unsuitable to host pentachloroethane molecules.

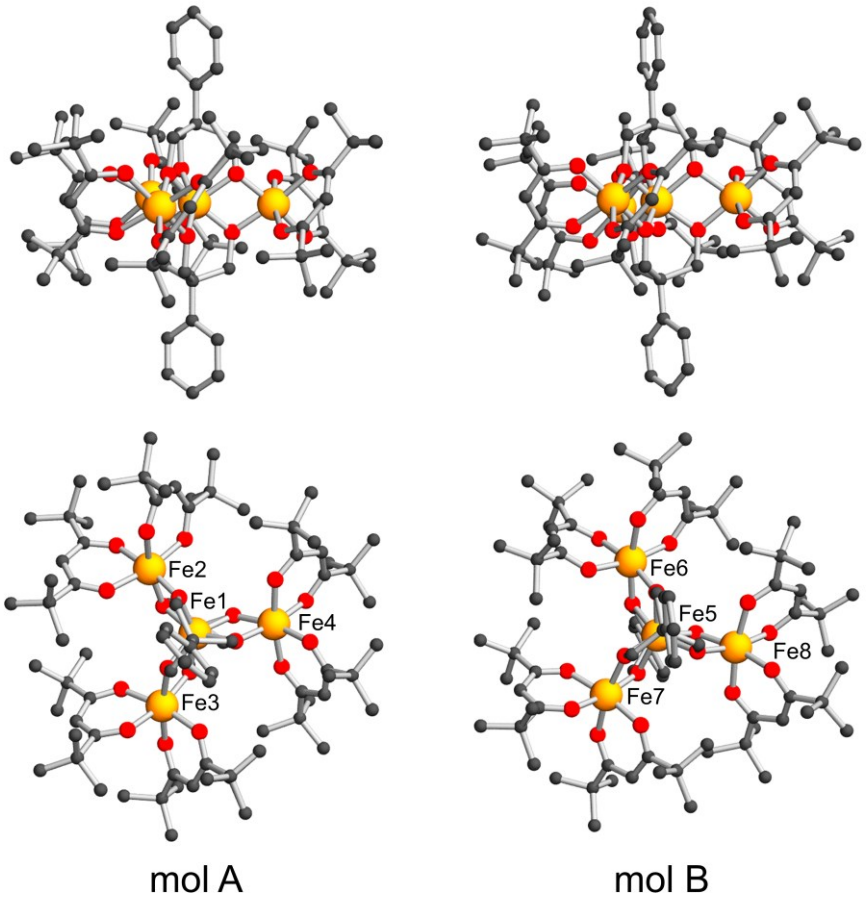

Fig. 2. Side (upper figures) and top (lower figures) views of the two crystallographically independent molecules in **1**: mol A (left) and mol B (right). Color code is the same as in Fig. 1. Disorder effects and H atoms are omitted for clarity.

Structure and magnetization dynamics of sublimated samples. Samples of **1**·C_7H_8, **1**·2CCl_4, **1**·C_6H_6, and unsolvated **1** were subject to thermal sublimation in HV at 450 - 490 K for a time sufficient to collected 1-2 mg of sublimated material on Teflon® tape. X-ray powder diffraction was used to get insight into the structure of these films. The low-angle (2θ = 5.5 - 20°) diffraction patterns are presented in Fig. 3. Apart from the signals of Teflon® at 16.37 and 18.20°, the sample prepared from unsolvated **1** gives only two very weak diffraction peaks between 9 and 10° and is thus predominantly amorphous. The deposits obtained from the three solvatomorphs **1**·C_7H_8, **1**·2CCl_4, and **1**·C_6H_6 feature dominant diffraction peaks at 6.78(3) and 9.51(2)°, which highlight structural similarities betweeen the samples. However, a set of weaker signals is also observed, which differ from sample to sample. For the sample obtained by sublimation of **1**·C_7H_8, the diffraction pattern agrees closely with the simulated pattern based on the structure of unsolvated **1** at room temperature (Fig. 3). However, sublimation of the tetrachloromethane and benzene solvates yields patterns which differ from that of the structurally characterized unsolvated phase. We have at present no definite explanation for such erratic behavior.

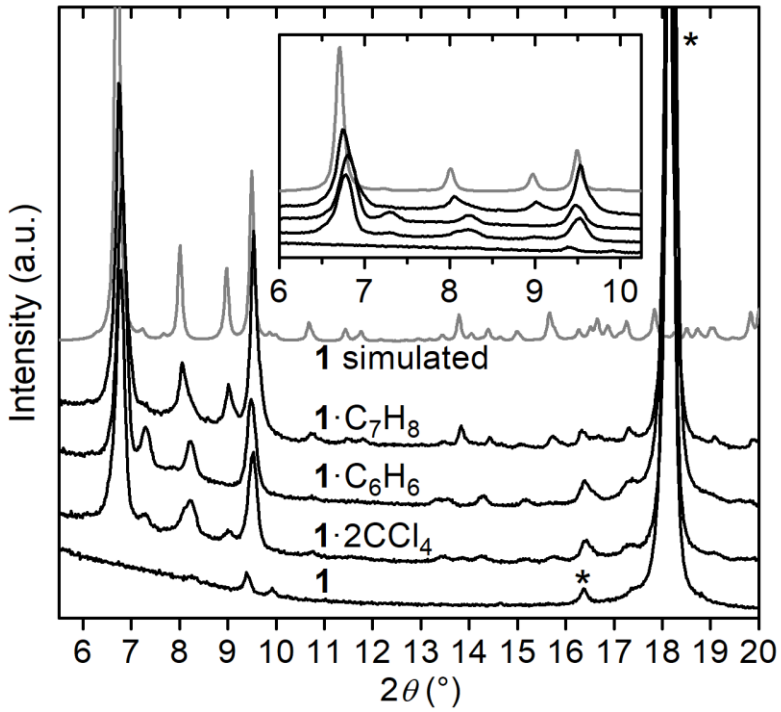

Fig. 3. Room-temperature powder diffractograms of sublimated films (black). Peaks marked with an asterisk are due to Teflon®. The inset shows a magnified view of the diffractograms below 2θ = 10°. The grey line is the expected pattern for **1** based on the crystal structure at 298 K.

The dynamics of the magnetization of the deposits was investigated using frequency- and temperature-dependent AC susceptibility measurements. The same technique was used to

characterize microcrystalline **1**. With no static field applied, sublimated **1** displays a frequency dependent, non-zero χ_M'' but no peaks appear within our experimental frequency window (Fig. S1). Upon application of a 1 kOe static field, relaxation slows down and a set of frequency and temperature dependent peaks become clearly visible (Fig. S2), indicating a thermally activated reversal of the magnetic moment. Sublimated material prepared from **1**·C_7H_8, **1**·2CCl_4, and **1**·C_6H_6 behaves similarly (Fig. S1 and S2). Extraction of the relaxation times through an extended Debye model allowed to prepare the Arrhenius plots reported in Fig. 4a. The linear fitting of the different thermal relaxation profiles yielded the parameters gathered in Fig. 4b and Table S3, which immediately highlight a strict resemblance of relaxation behavior between the different samples. Irrespective of the particular compound used, the deposits have τ_0 and Δ values comparable to microcrystalline **1**. Upon closer inspection of Fig. 4b, it can be seen that the activation parameters of sublimated **1** and **1**·C_6H_6 are within experimental error from those of microcrystalline **1**. Sublimated **1**·2CCl_4 has a slightly larger τ_0, whereas the deposit prepared from **1**·C_7H_8 has a significantly larger τ_0 and a reduced Δ, suggesting more efficient through-barrier relaxation.

Fig. S3 and S4 show the temperature dependence of the width parameter α and of the $(\chi_T-\chi_S)/\chi_T$ ratio, respectively. The latter allows to evaluate the molar fraction of slowly relaxing species. The results confirm a substantially uniform magnetic dynamics throughout the series and a modest dependence of the AC properties of sublimated samples on the used pristine material. In particular, at 1.8 K the values of α and $(\chi_T-\chi_S)/\chi_T$ span a remarkably limited range in all samples, including microcrystalline **1** (0.17-0.21 and 0.87-0.92, respectively). Differences between samples are enhanced upon heating to 2.4 K, with an overall tendency of α in sublimated samples to decrease more than in microcrystalline **1**. No clear correlation appears between α and the crystallinity of the films (Fig. 3). This is reasonable, since crystallinity reflects long-range ordering while the distribution width of relaxation times is primarily sensitive to the inhomogeneity of local molecular environments.

Our findings confirm the robustness of the tetrairon(III) core, which is able to sustain the high temperature and long heating times required by the sublimation protocol with only modest effects on magnetization dynamics.

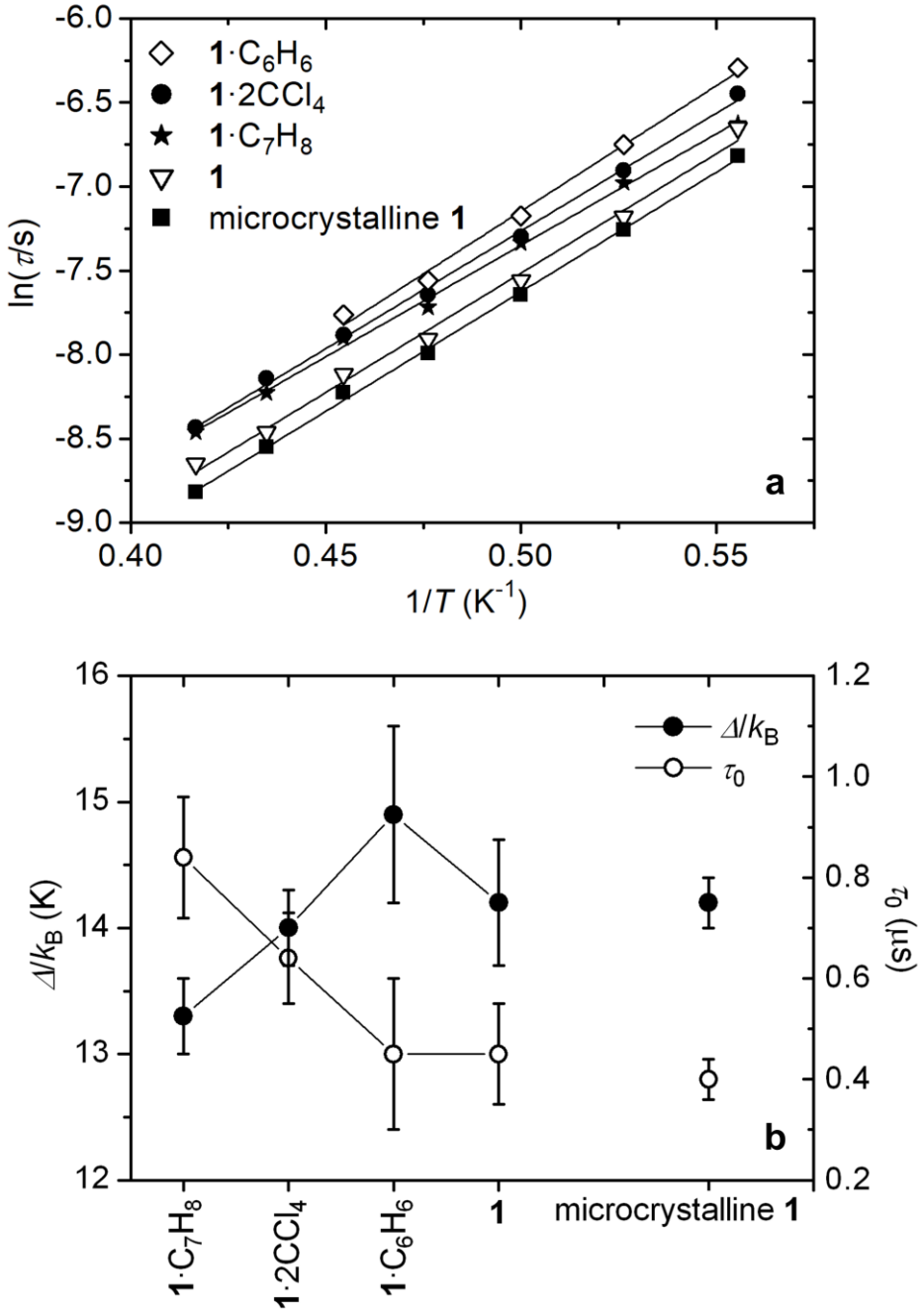

Fig. 4. Arrhenius plots of sublimated samples and of microcrystalline **1** at H_{DC} = 1 kOe (a), and graphical representation of the best-fit activation parameters (Δ and τ_0) so obtained (b). The vertical bars in (b) represent standard errors.

4. Conclusions

The series of known solvatomorphs of tetrairon(III) SMM $[Fe_4(L^{Ph})_2(dpm)_6]$ (**1**), namely **1**·Et_2O [26] and **1**·C_6H_6 [34], was extended with the isolation of **1**·C_7H_8 and **1**·$2CCl_4$. In addition, a solvent-free phase **1** was prepared by crystallization from pentachloroethane, a bulky solvent. The X-ray structures indicate that the most important structural parameter in these propeller-like species, namely the helical pitch, is distinctly different in solvatomorphs and in unsolvated **1**. Thus, intermolecular

interactions and crystal packing effects are crucial factors in determining molecular geometry. All compounds can be thermally sublimated in HV to give deposits displaying a variable degree of crystallinity. Most important, all sublimated samples show AC magnetic properties comparable to those of microcrystalline **1** in terms of activation parameters, fraction of slowly relaxing species and width of the distribution of relaxation times, irrespective of the pristine compound used. We conclude that molecular structure has the greatest impact on the vapor-phase processability of this class of materials.

SUPPLEMENTARY MATERIAL

Table S1. Crystal data and refinement parameters for compounds **1**·C_7H_8, **1**·2CCl_4 and **1**

	1·C_7H_8	**1**·2CCl_4	**1**
Formula	$C_{93}H_{144}Fe_4O_{18}$	$C_{88}H_{136}Cl_8Fe_4O_{18}$	$C_{86}H_{136}Fe_4O_{18}$
Formula weight	1773.48	1988.96	1681.35
T, K	140(2)	140(2)	150(2)
λ, Å	0.71073	0.71073	0.71073
Crystal size, mm^3	0.47×0.26×0.25	0.44×0.23×0.17	0.55×0.40×0.20
Crystal system	monoclinic	monoclinic	monoclinic
Space group	*C*2/*c* (No. 15)	*C*2/*c* (No. 15)	$P2_1/c$ (No. 14)
a, Å	19.3750(15)	19.6741(6)	21.9792(14)
b, Å	22.1147(16)	22.0496(6)	32.6985(19)
c, Å	24.403(2)	25.2684(6)	26.3903(17)
β, deg	109.099(2)	110.7367(9)	99.947(3)
V, $Å^3$	9880.6(13)	10251.5(5)	18681(2)
Z	4	4	8
D_{calcd}, g cm^{-3}	1.192	1.289	1.196
μ(Mo-Kα), mm^{-1}	0.636	0.822	0.669
F(000)	3800	4192	7200
θ range, deg	2.68-28.03	2.93-26.00	1.68-27.56
Reflns collected	52853	46809	190546
R_{int}	0.0286	0.0283	0.0346
Data/restraints/parameters	11944/63/529	9939/121/606	42925/6/1959
Goodness-of-fit on F^2	1.037	1.037	1.006
Final R indices [I>2σ(I)]	$R1$ = 0.0419, $wR2$ = 0.1107	$R1$ = 0.0442, $wR2$ = 0.1195	$R1$ = 0.0404, $wR2$ = 0.0987
R indices (all data)	$R1$ = 0.0578, $wR2$ = 0.1256	$R1$ = 0.0553, $wR2$ = 0.1283	$R1$ = 0.0706, $wR2$ = 0.1152
Largest diff. peak/hole, $eÅ^{-3}$	0.801 / –0.605	1.090 / –0.513	0.702 / –0.473

Table S2. Selected geometrical parameters in compounds **1**·C_7H_8 (at 140 K), **1**·2CCl_4 (at 140 K), **1**·Et_2O (at 203 K), **1**·C_6H_6 (at 120 K) and **1** (at 150 K)

		1·C_7H_8	**1**·2CCl_4	**1**·Et_2O [a]	**1**·C_6H_6 [b]
Fe1···Fe2 (Å)		3.0797(6)	3.0824(6)	3.0780(8)	3.0789(8)
Fe1···Fe3 (Å)		3.0783(4)	3.0780(4)	3.0726(6)	3.0764(5)
Fe2···Fe3 (Å)		5.3137(5)	5.3385(5)	5.2925(7)	5.3029(7)
Fe3···Fe3' (Å)		5.3695(7)	5.3245(7)	5.3880(11)	5.3827(8)
Fe_c–O (Å)		1.97-1.98	1.98	1.96-1.98	1.98-1.99
Fe_p–O (Å)		1.97-2.04	1.97-2.02	1.97-2.03	1.97-2.02
Fe_c–O–Fe_p (°)		102.1-102.2	102.0-102.3	102.0-102.4	102.0-102.2
α (°) [c]		89.25	89.22	89.24	89.21
β (°) [c]		77.80	77.84	77.72	77.80
θ (°) [d]		54.21	54.19	54.20	54.18
ϕ (°) [d]		32.76	32.74	32.51	32.62
γ_{cp} (°)	$Fe1(O)_2Fe2$	68.51(5)	68.72(6)	68.79(7)	68.77(8)
	$Fe1(O)_2Fe3$	68.69(4)	68.64(5)	68.77(6)	68.71(6)
γ (°) [e]		68.63	68.67	68.78	68.73

	1, mol A			**1**, mol B		
Fe_c···Fe_p (Å)	Fe1···Fe2 3.0736(4)	Fe1···Fe3 3.0917(4)	Fe1···Fe4 3.0857(4)	Fe5···Fe6 3.0776(5)	Fe5···Fe7 3.0833(5)	Fe5···Fe8 3.0848(4)
Fe_p···Fe_p (Å)	Fe2···Fe3 5.3642(5)	Fe3···Fe4 5.3894(5)	Fe2···Fe4 5.2679(5)	Fe6···Fe7 5.3227(5)	Fe7···Fe8 5.3968(5)	Fe6···Fe8 5.2930(5)
Fe_c–O (Å)	1.97-1.99			1.97-1.99		
Fe_p–O (Å)	1.97-2.01			1.97-2.01		
Fe_c–O–Fe_p (°)	102.1-103.2			101.9-102.5		
α (°) [c]	88.89			88.83		
β (°) [c]	77.47			77.64		
θ (°) [d]	53.95			53.91		
ϕ (°) [d]	30.51			30.79		
γ_{cp} (°)	$Fe1(O)_2Fe2$ 70.61(4)	$Fe1(O)_2Fe3$ 69.33(4)	$Fe1(O)_2Fe4$ 70.41(4)	$Fe5(O)_2Fe6$ 70.73(4)	$Fe5(O)_2Fe7$ 69.86(4)	$Fe5(O)_2Fe8$ 69.37(4)
γ (°) [e]	70.12			69.99		

[a]Data taken from Ref.[26]. [b]Data taken from Ref.[34]. [c]After D_3 symmetry averaging, α and β are the O-Fe-O interbond angles involving the central Fe^{3+} ion and O atoms related by three-fold rotation (α) or bridging to the same peripheral Fe^{3+} ion (β). [d]The angles θ and ϕ describe the distortion of the coordination sphere of Fe_c (averaged to D_3 symmetry) by trigonal compression/elongation and trigonal rotation, respectively. The extent of distortion is measured by the deviation of these angles from octahedral values (54.74 and 60°, respectively). [e]Average value of γ_{cp}. For details, see Refs. [25,43,44].

Table S3. Best-fit activation parameters extracted from Arrhenius plots of sublimated samples and of microcrystalline **1** at H_{DC} = 1 kOe. Numbers in parentheses are standard errors on the last significant digit.

	1·C_7H_8	**1**·2CCl_4	**1**·C_6H_6	**1**	microcrystalline **1**
τ_0 (s)	8.4(12)·10^{-7}	6.4(9)·10^{-7}	4.5(15)·10^{-7}	4.5(10)·10^{-7}	4.0(4)·10^{-7}
Δ/k_B (K)	13.3(3)	14.0(3)	14.9(7)	14.2(5)	14.2(2)

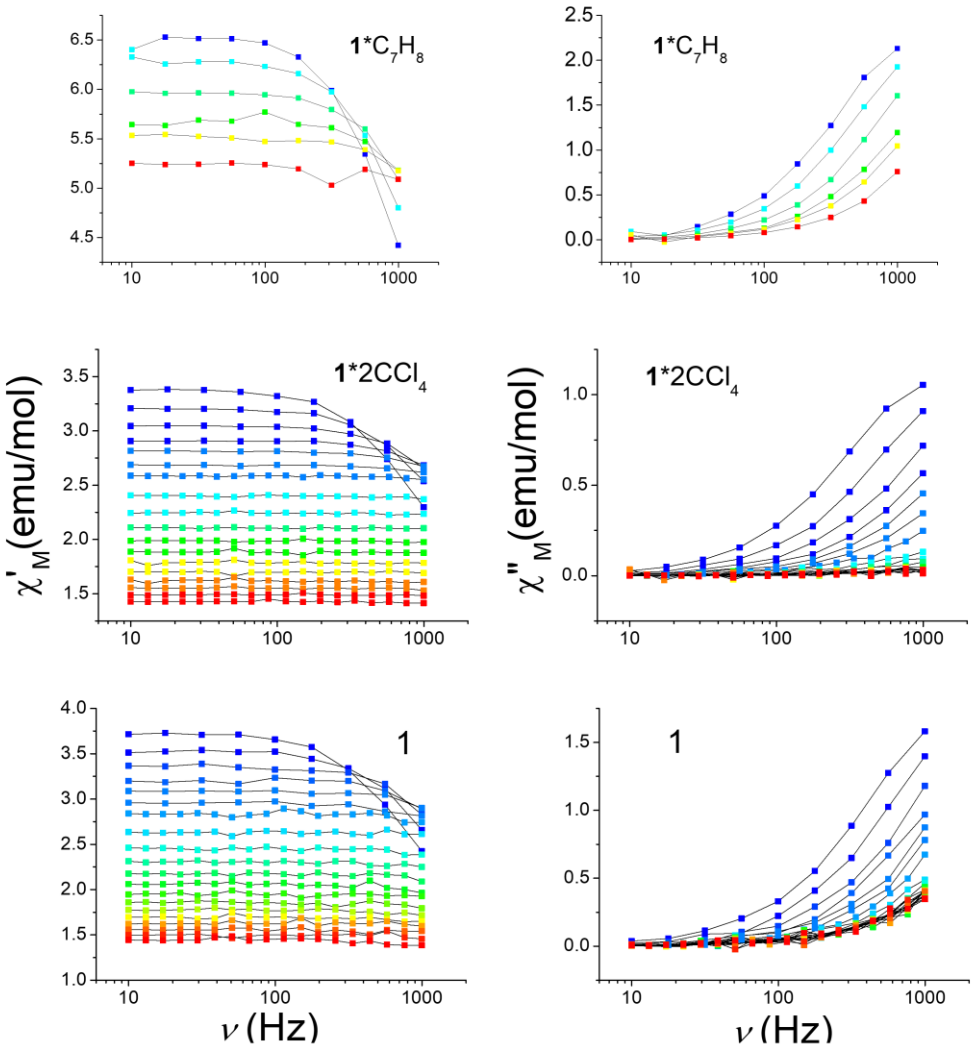

Fig. S1. Isothermal frequency dependence of the in-phase (χ_M') and out-of-phase (χ_M'') molar magnetic susceptibilities measured at H_{DC} = 0 on sublimated samples prepared from **1**·C_7H_8, **1**·2CCl_4 and **1**. Temperature spans the range from 1.8 K (blue points) to 5.0 K (red points) for **1**·2CCl_4 and **1**, and from 1.8 to 2.3 K for **1**·C_7H_8.

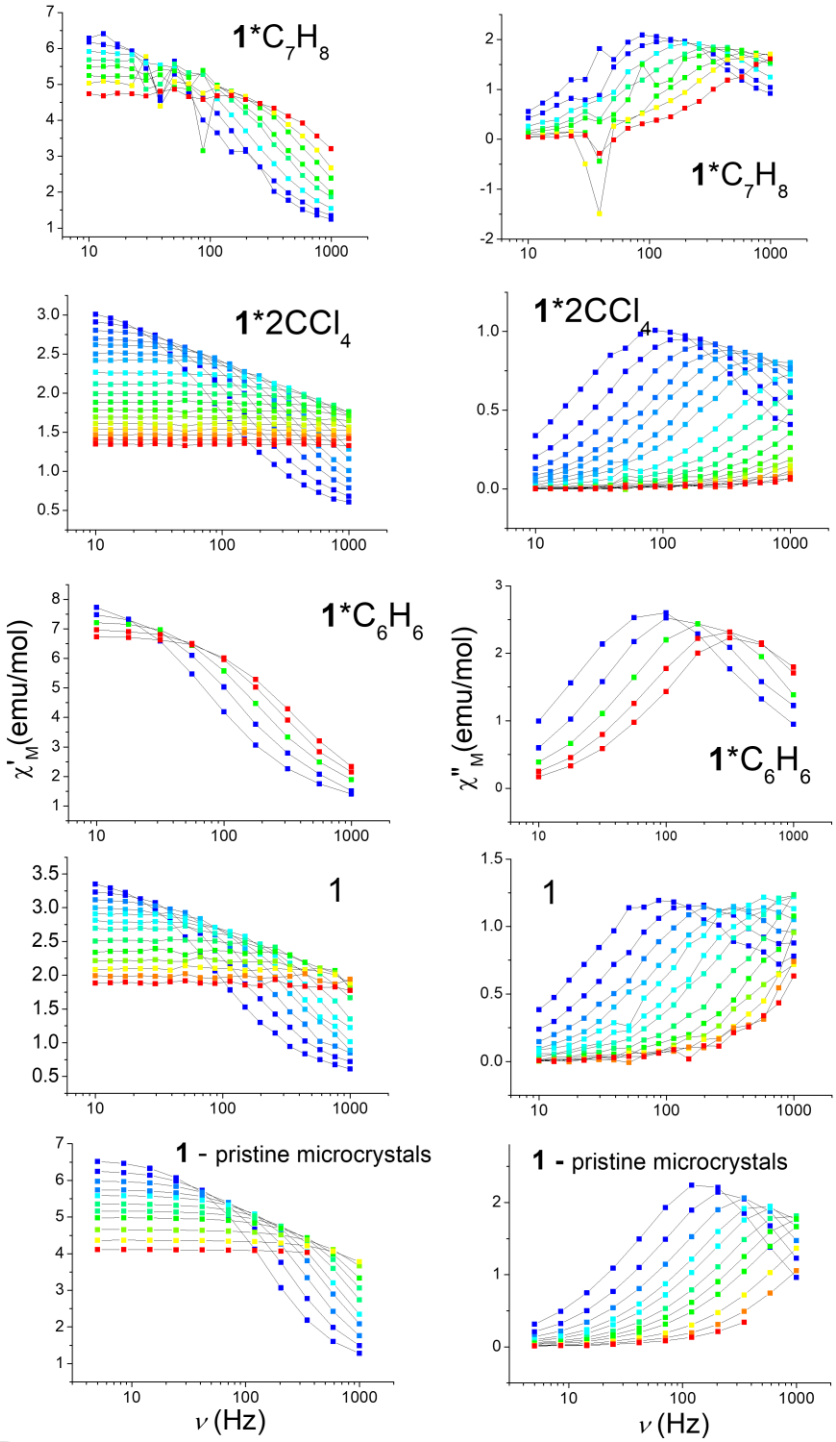

Fig. S2. Isothermal frequency dependence of the in-phase (χ_M') and out-of-phase (χ_M'') molar magnetic susceptibilities measured at H_{DC} = 1 kOe on sublimated samples and on microcrystalline **1**. Temperature spans the range from 1.8 K (blue points) to 5.0 K (red points) for all the investigated samples but **1**·C_6H_6, where the red dots identify the 2.2 K data.

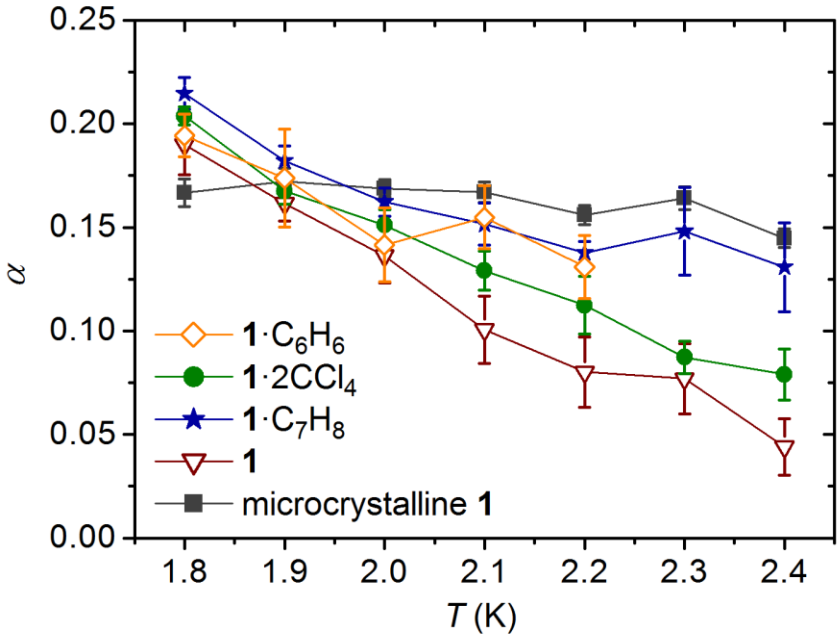

Fig. S3. Temperature dependence of the width parameter α for sublimated samples and for microcrystalline **1**, evaluated by fitting the Cole-Cole plots at H_{DC} = 1 kOe.

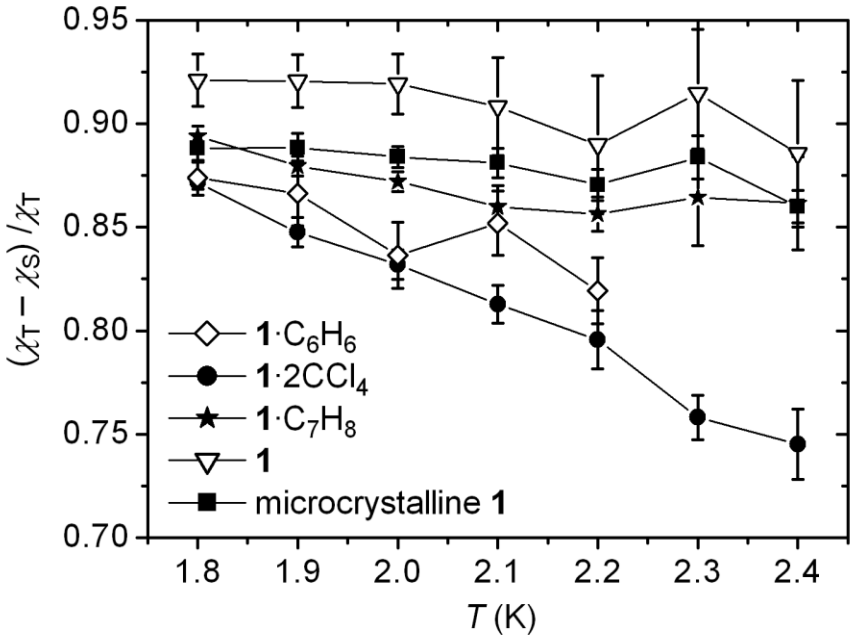

Fig. S4. Temperature dependence of the $(\chi_T-\chi_S)/\chi_T$ ratio for sublimated samples and for microcrystalline **1**, evaluated by fitting the Cole-Cole plots at H_{DC} = 1 kOe.

Acknowledgements

The authors thank Dr. Luca Rigamonti for preliminary studies and assistance in the preparation of bulk samples, and Brunetto Cortigiani for his assistance in the setup of the sublimation chambers used in this work. G.P. gratefully acknowledges FAPERJ for financial support through grants E-26/202.912/2019, SEI-260003/001167/2020 and E-26/010.000978/2019.

References

[1] R.J. Holmberg, M. Murugesu, Adhering magnetic molecules to surfaces, J. Mater. Chem. C. 3 (2015) 11986–11998. https://doi.org/10.1039/C5TC03225C.

[2] A. Cornia, D.R. Talham, M. Affronte, Thin Layers of Molecular Magnets, in: B. Sieklucka, D. Pinkowicz (Eds.), Mol. Magn. Mater. Concepts Appl., Wiley-VCH, Weinheim, 2017: pp. 187–229. https://doi.org/10.1002/9783527694228.

[3] A. Forment-Aliaga, E. Coronado, Hybrid Interfaces in Molecular Spintronics, Chem. Rec. 18 (2018) 737–748. https://doi.org/10.1002/tcr.201700109.

[4] F. Ara, H. Oka, Y. Sainoo, K. Katoh, M. Yamashita, T. Komeda, Spin properties of single-molecule magnet of double-decker Tb(III)-phthalocyanine (TbPc2) on ferromagnetic Co film characterized by spin polarized STM (SP-STM), J. Appl. Phys. 125 (2019) 183901. https://doi.org/10.1063/1.5079964.

[5] F.-S. Guo, B.M. Day, Y.-C. Chen, M.-L. Tong, A. Mansikkamäki, R.A. Layfield, Magnetic hysteresis up to 80 kelvin in a dysprosium metallocene single-molecule magnet, Science (80-.). 362 (2018) 1400–1403. https://doi.org/10.1126/science.aav0652.

[6] C.A.P. Goodwin, F. Ortu, D. Reta, N.F. Chilton, D.P. Mills, Molecular magnetic hysteresis at 60 kelvin in dysprosocenium, Nature. 548 (2017) 439–442. https://doi.org/10.1038/nature23447.

[7] F.-S. Guo, B.M. Day, Y.-C. Chen, M.-L. Tong, A. Mansikkamäki, R.A. Layfield, A Dysprosium Metallocene Single-Molecule Magnet Functioning at the Axial Limit, Angew. Chemie Int. Ed. 56 (2017) 11445–11449. https://doi.org/10.1002/anie.201705426.

[8] R. Sessoli, Magnetic molecules back in the race, Nature. 548 (2017) 400–401. https://doi.org/10.1038/548400a.

[9] T. Komeda, K. Katoh, M. Yamashita, Double-decker phthalocyanine complex: scanning tunneling microscopy study of film formation and spin properties, Prog. Surf. Sci. 89 (2014) 127–160. https://doi.org/10.1016/j.progsurf.2014.03.001.

[10] Y. Zhang, P. Liao, J. Kan, C. Yin, N. Li, J. Liu, Q. Chen, Y. Wang, W. Chen, G.Q. Xu, J. Jiang, R. Berndt, K. Wu, Low-temperature scanning tunneling microscopy study on the electronic properties of a double-decker DyPc2 molecule at the surface., Phys. Chem. Chem.

Phys. 17 (2015) 27019–27026. https://doi.org/10.1039/c5cp03925h.

[11] A. Lodi Rizzini, C. Krull, A. Mugarza, T. Balashov, C. Nistor, R. Piquerel, S. Klyatskaya, M. Ruben, P.M. Sheverdyaeva, P. Moras, C. Carbone, C. Stamm, P.S. Miedema, P.K. Thakur, V. Sessi, M. Soares, F. Yakhou-Harris, J.C. Cezar, S. Stepanow, P. Gambardella, Coupling of single, double, and triple-decker metal-phthalocyanine complexes to ferromagnetic and antiferromagnetic substrates, Surf. Sci. 630 (2014) 361–374. https://doi.org/10.1016/j.susc.2014.07.008.

[12] L. Malavolti, L. Poggini, L. Margheriti, D. Chiappe, P. Graziosi, B. Cortigiani, V. Lanzilotto, F. Buatier de Mongeot, P. Ohresser, E. Otero, F. Choueikani, P. Sainctavit, I. Bergenti, V.A. Dediu, M. Mannini, R. Sessoli, Magnetism of TbPc2 SMMs on ferromagnetic electrodes used in organic spintronics, Chem. Commun. 49 (2013) 11506–11508. https://doi.org/10.1039/c3cc46868b.

[13] D. Klar, A. Candini, L. Joly, S. Klyatskaya, B. Krumme, P. Ohresser, J.-P. Kappler, M. Ruben, H. Wende, Hysteretic behaviour in a vacuum deposited submonolayer of single ion magnets, Dalton Trans. 43 (2014) 10686–10689. https://doi.org/10.1039/c4dt01005a.

[14] L. Margheriti, D. Chiappe, M. Mannini, P.-E. Car, P. Sainctavit, M.-A. Arrio, F. Buatier de Mongeot, J.C. Cezar, F.M. Piras, A. Magnani, E. Otero, A. Caneschi, R. Sessoli, X-ray detected magnetic hysteresis of thermally evaporated terbium double-decker oriented films, Adv. Mater. 22 (2010) 5488–5493. https://doi.org/10.1002/adma.201003275.

[15] J. Dreiser, C. Wäckerlin, M.E. Ali, C. Piamonteze, F. Donati, A. Singha, K.S. Pedersen, S. Rusponi, J. Bendix, P.M. Oppeneer, T.A. Jung, H. Brune, Exchange interaction of strongly anisotropic tripodal erbium single-ion magnets with metallic surfaces, ACS Nano. 8 (2014) 4662–4671. https://doi.org/10.1021/nn500409u.

[16] J. Dreiser, G.E. Pacchioni, F. Donati, L. Gragnaniello, A. Cavallin, K.S. Pedersen, J. Bendix, B. Delley, M. Pivetta, S. Rusponi, H. Brune, Out-of-Plane Alignment of Er(trensal) Easy Magnetization Axes Using Graphene, ACS Nano. 10 (2016) 2887–2892. https://doi.org/10.1021/acsnano.5b08178.

[17] J. Dreiser, C. Wäckerlin, M. Buzzi, K.S. Pedersen, J. Bendix, Island formation of Er(trensal) single-ion magnets on graphene observed on the micrometer scale, RSC Adv. 11 (2021) 9421–9425. https://doi.org/10.1039/D1RA00783A.

[18] S.G. Miralles, A. Bedoya-Pinto, J.J. Baldoví, W. Cañon-Mancisidor, Y. Prado, H. Prima-Garcia, A. Gaita-Ariño, G. Mínguez Espallargas, L.E. Hueso, E. Coronado, Sublimable chloroquinolinate lanthanoid single-ion magnets deposited on ferromagnetic electrodes, Chem. Sci. 9 (2018) 199–208. https://doi.org/10.1039/C7SC03463F.

[19] C. Gao, Q. Yang, B.-W. Wang, Z.-M. Wang, S. Gao, Evaporable lanthanide single-ion

magnet, CrystEngComm. 18 (2016) 4165–4171. https://doi.org/10.1039/C5CE02571K.

[20] Y. Bi, C. Chen, Y.-F. Zhao, Y.-Q. Zhang, S.-D. Jiang, B.-W. Wang, J.-B. Han, J.-L. Sun, Z.-Q. Bian, Z.-M. Wang, S. Gao, Thermostability and photoluminescence of Dy(III) single-molecule magnets under a magnetic field, Chem. Sci. 7 (2016) 5020–5031. https://doi.org/10.1039/C6SC01157H.

[21] K. Katoh, H. Isshiki, T. Komeda, M. Yamashita, Multiple-decker phthalocyaninato Tb(III) single-molecule magnets and Y(III) complexes for next generation devices, Coord. Chem. Rev. 255 (2011) 2124–2148. https://doi.org/10.1016/j.ccr.2011.02.024.

[22] X. Yi, K. Bernot, F. Pointillart, G. Poneti, G. Calvez, C. Daiguebonne, O. Guillou, R. Sessoli, A luminescent and sublimable DyIII-based single-molecule magnet, Chem. - A Eur. J. 18 (2012) 11379–11387. https://doi.org/10.1002/chem.201201167.

[23] E. Kiefl, M. Mannini, K. Bernot, X. Yi, A. Amato, T. Leviant, A. Magnani, T. Prokscha, A. Suter, R. Sessoli, Z. Salman, Robust Magnetic Properties of a Sublimable Single-Molecule Magnet, ACS Nano. 10 (2016) 5663–5669. https://doi.org/10.1021/acsnano.6b01817.

[24] D.S. Krylov, S. Schimmel, V. Dubrovin, F. Liu, T.T.N. Nguyen, L. Spree, C. Chen, G. Velkos, C. Bulbucan, R. Westerström, M. Studniarek, J. Dreiser, C. Hess, B. Büchner, S.M. Avdoshenko, A.A. Popov, Substrate-Independent Magnetic Bistability in Monolayers of the Single-Molecule Magnet Dy2ScN@C80 on Metals and Insulators, Angew. Chemie Int. Ed. 59 (2020) 5756–5764. https://doi.org/10.1002/anie.201913955.

[25] A. Cornia, M. Mannini, R. Sessoli, D. Gatteschi, Propeller-Shaped Fe4 and Fe3M Molecular Nanomagnets: A Journey from Crystals to Addressable Single Molecules, Eur. J. Inorg. Chem. 2019 (2019) 552–568. https://doi.org/10.1002/ejic.201801266.

[26] S. Accorsi, A.-L. Barra, A. Caneschi, G. Chastanet, A. Cornia, A.C. Fabretti, D. Gatteschi, C. Mortalò, E. Olivieri, F. Parenti, P. Rosa, R. Sessoli, L. Sorace, W. Wernsdorfer, L. Zobbi, Tuning anisotropy barriers in a family of tetrairon(III) single-molecule magnets with an S = 5 ground state, J. Am. Chem. Soc. 128 (2006) 4742–4755. https://doi.org/10.1021/ja0576381.

[27] L. Margheriti, M. Mannini, L. Sorace, L. Gorini, D. Gatteschi, A. Caneschi, D. Chiappe, R. Moroni, F. Buatier De Mongeot, A. Cornia, F.M. Piras, A. Magnani, R. Sessoli, Thermal deposition of intact tetrairon(III) single-molecule magnets in high-vacuum conditions, Small. 5 (2009) 1460–1466. https://doi.org/10.1002/smll.200801594.

[28] L. Malavolti, V. Lanzilotto, S. Ninova, L. Poggini, I. Cimatti, B. Cortigiani, L. Margheriti, D. Chiappe, E. Otero, P. Sainctavit, F. Totti, A. Cornia, M. Mannini, R. Sessoli, Magnetic bistability in a submonolayer of sublimated Fe4 single-molecule magnets, Nano Lett. 15 (2015) 535–541. https://doi.org/10.1021/nl503925h.

[29] V. Lanzilotto, L. Malavolti, S. Ninova, I. Cimatti, L. Poggini, B. Cortigiani, M. Mannini, F.

Totti, A. Cornia, R. Sessoli, The Challenge of Thermal Deposition of Coordination Compounds: Insight into the Case of an Fe4 Single Molecule Magnet, Chem. Mater. 28 (2016) 7693–7702. https://doi.org/10.1021/acs.chemmater.6b02696.

[30] J.A.J. Burgess, L. Malavolti, V. Lanzilotto, M. Mannini, S. Yan, S. Ninova, F. Totti, S. Rolf-Pissarczyk, A. Cornia, R. Sessoli, S. Loth, Magnetic fingerprint of individual Fe4 molecular magnets under compression by a scanning tunnelling microscope, Nat. Commun. 6 (2015) 8216. https://doi.org/10.1038/ncomms9216.

[31] L. Rigamonti, M. Piccioli, L. Malavolti, L. Poggini, M. Mannini, F. Totti, B. Cortigiani, A. Magnani, R. Sessoli, A. Cornia, Enhanced vapor-phase processing in fluorinated Fe4 single-molecule magnets, Inorg. Chem. 52 (2013) 5897–5905. https://doi.org/10.1021/ic400037c.

[32] S. Ninova, V. Lanzilotto, L. Malavolti, L. Rigamonti, B. Cortigiani, M. Mannini, F. Totti, R. Sessoli, Valence electronic structure of sublimated Fe4 single-molecule magnets: an experimental and theoretical characterization, J. Mater. Chem. C. 2 (2014) 9599–9608. https://doi.org/10.1039/C4TC01647E.

[33] G. Serrano, L. Poggini, M. Briganti, A.L. Sorrentino, G. Cucinotta, L. Malavolti, B. Cortigiani, E. Otero, P. Sainctavit, S. Loth, F. Parenti, A.-L. Barra, A. Vindigni, A. Cornia, F. Totti, M. Mannini, R. Sessoli, Quantum dynamics of a single molecule magnet on superconducting Pb(111), Nat. Mater. 19 (2020) 546–551. https://doi.org/10.1038/s41563-020-0608-9.

[34] L. Vergnani, A.-L. Barra, P. Neugebauer, M.J. Rodriguez-Douton, R. Sessoli, L. Sorace, W. Wernsdorfer, A. Cornia, Magnetic Bistability of Isolated Giant-Spin Centers in a Diamagnetic Crystalline Matrix, Chem. - A Eur. J. 18 (2012) 3390–3398. https://doi.org/10.1002/chem.201103251.

[35] W.L.F. Armarego, C.L.L. Chai, Purification of laboratory chemicals, 5th ed., Butterworth-Heinemann, Burlington, United States, 2003.

[36] B.S. Furniss, A.J. Hannaford, P.W.G. Smith, A.R. Tatchell, Vogel's Textbook of Practical Organic Chemistry, 5th ed., Longman Scientific & Technical, New York, United States, 1989.

[37] A. Altomare, G. Cascarano, C. Giacovazzo, A. Guagliardi, M.C. Burla, G. Polidori, M. Camalli, SIR 92 – a program for automatic solution of crystal structures by direct methods, J. Appl. Crystallogr. 27 (1994) 435–435. https://doi.org/10.1107/S002188989400021X.

[38] G.M. Sheldrick, Crystal structure refinement with SHELXL, Acta Crystallogr. Sect. C Struct. Chem. 71 (2015) 3–8. https://doi.org/10.1107/S2053229614024218.

[39] L.J. Farrugia, WinGX and ORTEP for Windows: an update, J. Appl. Crystallogr. 45 (2012) 849–854. https://doi.org/10.1107/S0021889812029111.

[40] Persistence of Vision Pty. Ltd., Persistence of Vision Raytracer (Version 3.7) [Computer software], retrieved from http://www.povray.org/download/, 2021. www.povray.org.

[41] C.F. Macrae, I. Sovago, S.J. Cottrell, P.T.A. Galek, P. McCabe, E. Pidcock, M. Platings, G.P. Shields, J.S. Stevens, M. Towler, P.A. Wood, Mercury 4.0 : from visualization to analysis, design and prediction, J. Appl. Crystallogr. 53 (2020) 226–235. https://doi.org/10.1107/S1600576719014092.

[42] C. V. Topping, S.J. Blundell, A.C. susceptibility as a probe of low-frequency magnetic dynamics, J. Phys. Condens. Matter. 31 (2019) 013001. https://doi.org/10.1088/1361-648X/aaed96.

[43] L. Gregoli, C. Danieli, A.-L. Barra, P. Neugebauer, G. Pellegrino, G. Poneti, R. Sessoli, A. Cornia, Magnetostructural correlations in tetrairon(III) single-molecule magnets, Chem. - A Eur. J. 15 (2009) 6456–6467. https://doi.org/10.1002/chem.200900483.

[44] J. Mayans, M. Font-Bardia, A. Escuer, Chiroptical and magnetic properties of star-shaped FeIII4 complexes from chiral Schiff bases. Structural and magnetic correlations based on continuous shape measures, Dalt. Trans. 47 (2018) 8392–8401. https://doi.org/10.1039/C8DT01684D.